Optimal Wireless Power Transfer with Distributed Transmit Beamforming

Rui Wang and D. Richard Brown III

Abstract: **This paper considers the performance of wireless power transfer (WPT) with distributed transmit beamforming (DTB) in a narrowband setting. One or more receive nodes, each equipped with energy harvesting and storage capabilities, provide periodic channel state feedback to a cluster of transmit nodes, each with an independent local oscillator, to facilitate beamforming and passband signal alignment for efficient WPT. Without channel state feedback, the transmit cluster can not align the passband signals at the receivers and the receivers can only harvest incoherent power. Since feedback improves the beamforming gain but requires the receivers to expend energy, there is a fundamental tradeoff between the feedback period and the energy harvesting efficiency. This paper analyzes the optimal feedback period to maximize the weighted mean energy harvesting rate as a function of the oscillator parameters. An optimization problem is formulated and an explicit method to numerically calculate the globally optimal feedback period is developed. Numerical results are provided to confirm the analysis and demonstrate the sensitivity of the weighted mean energy harvesting rate with respect to the feedback period and the DTB system parameters.**

Index Terms: **Channel state feedback, distributed transmit beamforming, energy harvesting, oscillator dynamics, synchronization, wireless power transfer.**

I. INTRODUCTION

SINCE the invention of Tesla Coil in 1893 [1], there has been more than a century of research on methods for wirelessly transferring power using radio waves [2]. In recent years, the development of efficient radio frequency (RF) radiation wireless power transfer (WPT) systems has become an active research area, motivated in part by the widespread use of low-power devices that can be charged wirelessly [3]. An example of WPT using RF radiation is the wireless identification and sensing platform (WISP) [4]. Other recent examples of WPT using RF radiation include harvesting energy from terrestrial television signals [4], cellular base station signals [5], and signals from wireless fidelity (Wi-Fi) routers [6].

Besides RF radiation, there are typically two other types of WPT techniques: Inductive coupling (IC) in low-frequency bands and magnetic resonant coupling (MRC) in high-frequency bands [7]. In inductive coupling, the transmitter and receiver coils together form a transformer and power is transferred between the coils by a magnetic field [8]. Inductive coupling is the most mature wireless power technology and is essentially the only technology so far which is used in commercial products such as charging of mobile phones, electric vehicles, and biomedical prosthetic devices implanted in the human body [9]–[12]. MRC is a form of inductive coupling in which power is transferred by magnetic fields between two resonant circuits, one in the transmitter and one in the receiver [13], [14]. Recently, MRC-based WPT (MRC-WPT) with multiple transmitters and/or multiple receivers has been studied in the literature [15]–[17]. The WiTricity system is an example of a standardized commercial MRC-WPT system.

A common feature of both IC-WPT and MRC-WPT is that they operate in the near-field. As such, the power strength is attenuated according to the cube of the reciprocal of the distance between the coils [18], [19], i.e., power is attenuated at 60 dB per decade. As a result, IC-WPT is typically used for short-range applications in centimeters [9], [20] and MRC-WPT is typically used for mid-range applications up to a couple of meters [13], [14]. RF-WPT, on the other hand, operates in the far field. While the amount of energy transfer for RF-WPT is typically smaller[1] than in IC-WPT and MRC-WPT, there are several potential advantages of RF-WPT. First, the signal strength of far-field RF transmission over a free-space link is attenuated according to the reciprocal of the distance between transmitter and receiver [22], i.e., power is attenuated at 20 dB per decade. As such, RF-WPT can be be more efficient than IC-WPT and MRC-WPT over longer range links and can be suitable for powering a larger number of devices distributed in a wide area. Second, RF-WPT does not require a large coil like IC-WPT and MRC-WPT. In fact, RF-WPT can use antennas already present in a device for wireless communications. Such antennas can also be used for power transfer or simultaneous wireless information and power transfer (SWIPT) [3]. These characteristics can make RF-WPT appealing in low-cost communication devices [23].

A disadvantage of all WPT techniques over longer ranges is that path loss effects can significantly reduce the amount of power received by energy harvesting devices. To overcome this problem, recent investigations have considered the use of transmit beamforming with RF-WPT, e.g., [24], [25]. To achieve coherency in a narrowband setting, the transmit array must have estimates of the channel phases to each receive node. This channel state information at the transmitter (CSIT) is typically obtained via feedback from the receive nodes. Alternatively, in systems with channel reciprocity, e.g., time-division duplexed

Manuscript received July 21, 2016; approved for publication by Sinan Gezici, Division II Editor, January 16, 2017.

This work was supported by the National Science Foundation awards CCF-1302104 and CCF-1319458.

The authors are with the Department of Electrical and Computer Engineering, Worcester Polytechnic Institute, Worcester MA 01609, USA, email: {rwang, drb}@wpi.edu.

Digital object identifier: 10.1109/JCN.2017.000023

[1] While RF-WPT is generally studied in the context of low-power applications, it has also been considered in scenarios with more substantial power requirements, e.g., [21].

(TDD) channels, CSIT can be obtained by having the transmitter directly estimate the channel phases from periodic sounding signals transmitted by the receive nodes. Irrespective of the method in which the CSIT is obtained, the transmit array uses the CSIT to adjust the phases of the passband transmissions so that the signals constructively combine at the intended receiver and the efficiency of WPT is improved.

Recently, researchers have considered the use of *distributed* transmit beamforming (DTB) in wireless communication systems where two or more individual transmit nodes pool their antenna resources to emulate a virtual antenna array [26]. In principle, the distributed array works in the same way as the conventional (centralized) array: the individual transmit nodes use the CSIT obtained either by feedback ("feedback-based" DTB, e.g., [27]–[32]) or through channel reciprocity ("reciprocity-based" DTB, e.g., [33], [34]) to form a beam by controlling the phase of their passband transmissions so that the signals constructively combine at an intended receive node. Unlike conventional transceivers, however, a distributed transmit beamformer naturally allows for low-cost deployment of robust large-aperture arrays suitable for efficient wireless communications and WPT.

Another distinction between conventional transmit beamforming and DTB is that each node in a distributed beamformer has an *independent local oscillator*. It is generally assumed in these settings that there is no exogenous source of synchronization of sufficient accuracy to facilitate DTB available to the transmit nodes. Hence, the transmit nodes' local oscillators experience stochastic dynamics and the passband signals from each transmit node experience phase and frequency drift over time. The transmit nodes can correct for these effects using the CSIT obtained through feedback from the receive nodes (or by exploiting channel reciprocity). Nevertheless, even if the nodes obtain perfect CSIT, it is only a short matter of time until the independent oscillators drift apart and coherence is lost. Periodic feedback is required to maintain coherence.

In this paper, we consider the use of DTB for WPT. While DTB has been studied extensively in the context of wireless communications (including reports of successful implementations, e.g., [35]), and also studied recently in the context of SWIPT [36], [37], to the best of our knowledge there has been no study of DTB for WPT accounting for (i) the cost of measuring and tracking CSIT and (ii) the effects of time-varying imperfect CSIT caused by tracking errors and oscillator dynamics. While [36], [37] both consider WPT in the context of DTB, these studies focus on SWIPT optimization problems like optimal power splitting under the assumption of perfect CSIT. In this paper, we study the *fundamental tradeoff* between the feedback period and the efficiency of the WPT system as shown notionally in Fig. 1. We show that there exists optimal feedback period such that the receivers can maximize their *net* mean energy harvesting rate after the cost of feedback and accounting for losses due to errors in the channel state information. This paper is focused on the question of how to find a globally optimal feedback period to maximize the mean energy harvesting rate at the receivers. While the focus of this paper is on WPT, we note that the techniques developed in this paper naturally extend to SWIPT since DTB has been extensively studied in the wireless communications context.

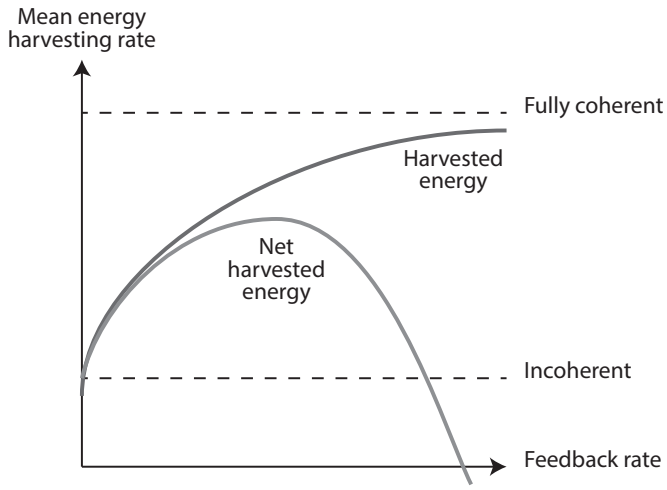

Fig. 1. Fundamental tradeoff between the feedback rate and the mean energy harvesting rate of the WPT system. The net harvested energy accounts for the cost of feedback.

The DTB WPT problem is different from the DTB communications problem due to the fundamental tradeoff between the feedback period and the efficiency of the WPT system as shown notionally in Fig. 1. The main contributions of this paper are summarized as follows:

- We develop a new model for WPT with DTB, explicitly accounting for losses caused by imperfect channel state information and independent oscillator dynamics and also accounting for the cost of feedback energy from the receive nodes.
- We formulate a "normalized weighted mean energy harvesting rate" (NWMEHR) maximization problem to select the feedback period to maximize the weighted averaged amount of net energy harvested by the receive nodes per unit of time as a function of the oscillator parameters. By maximizing the NWMEHR, the receive nodes maximize the *net* weighted harvested energy after feedback.
- Since the NWMEHR objective function is non-convex and implicit (involving the solution of a discrete-time algebraic Riccati equation), we develop an explicit method to numerically calculate the globally optimal feedback period. Our method solves the problem in two steps: (i) Bounding the search region into a closed interval and (ii) applying the DIRECT algorithm [38] on the bounded search region to find the globally optimal solution.

Our approach is distinguished from the prior work by the fact that we explicitly consider the effect of time-varying errors in the channel state information caused by tracking errors and independent local oscillators and also account for the cost of feedback energy in the WPT setting. This reveals the fundamental tradeoff shown in Fig. 1, the precise formulation of the NWMEHR optimization problem, and an explicit method to optimize the net harvested energy as a function of the oscillator parameters.

The remainder of this paper is organized as follows. Section II presents the system models for "feedback-based" DTB and formulates the NWMEHR maximization problem. Section III introduces forward link channel tracking and pre-

diction. Section IV analyzes the NWMEHR optimization problem and develops an efficient method to numerically solve it. Section V provides simulation results to confirm the analysis and demonstrate the effect of the system parameters on the achieved NWMEHR.

Notation: Boldface letters refer to vectors (lower case) or matrices (upper case). $\mathbb{N}^+$, $\mathbb{R}$, and $\mathbb{R}^{a\times b}$ denote the nonzero natural numbers, real numbers, and the space of $a\times b$ matrices with real entries, respectively. For a symmetric matrix $\boldsymbol{S}$, $\boldsymbol{S}\succ\boldsymbol{0}$ means that $\boldsymbol{S}$ is positive definite. For a square matrix $\boldsymbol{R}$, $|\boldsymbol{R}|$ denotes the determinant of $\boldsymbol{R}$. For an arbitrary-size matrix $\boldsymbol{M}$, $\|\boldsymbol{M}\|_F$ and $\boldsymbol{M}^{\mathrm{T}}$ denote the Frobenius norm and the transpose of $\boldsymbol{M}$, respectively. The distribution of a Gaussian random vector with mean μ and variance σ^2 is denoted by $\mathcal{N}(\mu,\sigma^2)$, and $\overset{\text{i.i.d.}}{\sim}$ denotes "independent and identically distributed as". $\mathbb{E}[\cdot]$ and cov denote the statistical expectation and covariance, respectively. $f(x)=O(g(x))$ for $x\to 0$ means that there exist constants $\epsilon>0$ and C such that $|f(x)|\le C|g(x)|$ for all x with $|x|<\epsilon$. For a set $A\subseteq\mathbb{R}$, $\int_{x\in A} f(x)\,dx$ denotes the integration of $f(x)$ over a specified domain A.

II. SYSTEM MODEL AND PROBLEM FORMULATION

In this section, we first introduce in Section II-A the system model and notation for the relevant parameters in "feedback-based" DTB. We then formulate the mean energy harvesting rate maximization problem in Section II-C.

For conciseness, our presentation focuses on "feedback-based" DTB. We point out, however, that the main concepts developed here also apply to "reciprocity-based" DTB since obtaining CSIT via reciprocity requires the receive nodes to periodically expend energy for reverse link channel sounding. While the details of the protocol and system parameters differ, both feedback-based DTB and reciprocity-based DTB possess the same fundamental tradeoff between the feedback rate (reverse link channel sounding rate) and WPT efficiency.

A. System Model

We assume a system with N_t transmit nodes and N_r receive nodes. All forward link channels are modeled as narrowband, linear, and time invariant (LTI). All nodes are assumed to possess a single isotropic antenna[2]. Adopting the convention that the transmit nodes are enumerated as $i=1,\cdots,N_t$ and the receive nodes are enumerated as $j=1,\cdots,N_r$, we denote the channel from transmit node i to receive node j as $g_{i,j}\in\mathbb{C}$. To facilitate beamforming toward the receive nodes in the forward link, we assume a "feedback-based" DTB protocol like [27]–[32] where the transmit nodes obtain CSIT through periodic forward link channel measurements and channel state feedback from the receive nodes on the reverse link. This protocol and its relevant parameters are illustrated in Fig. 2.

As shown in Fig. 2, each frame of the feedback-based DTB protocol has a duration of T_f and is composed of N_r slots. The j^{th} slot has a duration of $\mu_j T_f$, where the factors $\{\mu_j\}_{j=1}^{N_r}$ are

[2]Our focus on single antennas is motivated by clarity of exposition. The techniques developed in this paper can be extended to the case where nodes have more than one antenna at the expense of some additional notational complexity.

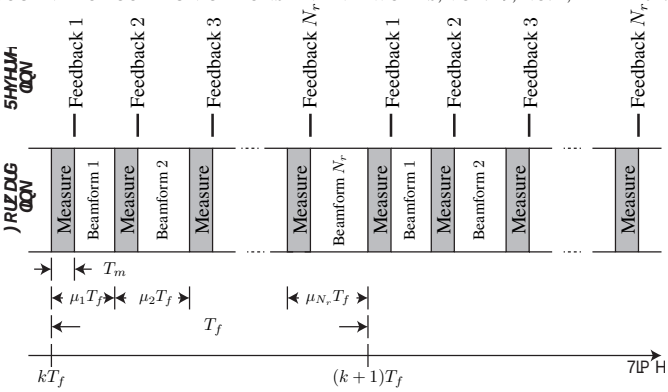

Fig. 2. Distributed transmit beamforming periodic protocol with frame period T_f.

all in the range $(0,1)$ and their summation is normalized to one, i.e., $\sum_{j=1}^{N_r}\mu_j=1$. Each slot contains a channel measurement interval followed immediately by a beamforming interval. During the channel measurement interval, each transmit node separately broadcasts a pilot of length T_0 (including any necessary guard times) to the receive nodes. The channel measurement interval length is then $T_m=N_tT_0$. All of the receive nodes use the pilots received during the channel measurement intervals to update their channel estimates. No beamforming or energy harvesting occurs during channel measurement intervals.

At the end of the channel measurement interval, a single receive node provides channel state feedback to the transmit cluster. The receive node is assumed to send L bits of information for each channel measurement and, hence, a receive node provides N_tL total bits of feedback in its slot. We assume the time required to send this feedback is small so that the beamforming interval to the receive node providing the feedback begins immediately after the measurement interval. During the beamforming interval of receive node j, receive node j harvests energy from the (approximately) coherent signals from the transmit cluster while all other receive nodes $\ell\in\{1,\cdots,N_r\}\backslash j$ harvest incoherent energy.

B. Harvested Energy Analysis

Receive nodes harvest approximately coherent energy during their beamforming interval and also harvest incoherent energy during the beamforming intervals of the other receive nodes. No energy is harvested during the channel measurement periods. We denote the beamforming power at the j^{th} receive node at time t as $J^{(j)}(t)$ and note that $J^{(j)}(t)$ is a stochastic process since the channel estimates are noisy and the independent clocks experience stochastic dynamics. We further denote the ensemble averaged beamforming power as $\overline{J}^{(j)}(t)=\mathbb{E}[J^{(j)}(t)]$. The total average energy harvested by the j^{th} receive node during the k^{th} frame period can be written as

$$E_b^{(j)}[k]=\eta\left[\int_{t\in\mathcal{T}_b^{(j)}[k]}\overline{J}^{(j)}\left(t-\sum_{s=1}^{j-1}\mu_sT_f\right)dt+P_{\text{inc}}^{(j)}\sum_{\substack{s=1\\ s\neq j}}^{N_r}(\mu_sT_f-T_m)\right],\qquad(1)$$

where $\eta \in (0,1)$ is the harvesting efficiency, $\mathcal{T}_b^{(j)}[k]$ is the beamforming interval in the j^{th} slot of the k^{th} frame, and $P_{\text{inc}}^{(j)}$ is the incoherent beamforming power at the j^{th} receive node. Note that this latter term accounts for the fact that the j^{th} receive node harvests incoherent beamforming power in the non-j^{th} beamforming slots. We further define the *steady-state* average energy harvested by the j^{th} receive node as $\overline{E}_b^{(j)} = \lim_{k\to\infty} E_b^{(j)}[k]$.

During the beamforming interval in the j^{th} slot, the transmitters attempt to align their phases so that the signals arrive with a common phase and combine coherently at the j^{th} receive node. We denote the signal at the j^{th} receive node from i^{th} transmit node as

$$r^{(i,j)}(t) = \sqrt{P_0}|g_{i,j}|e^{j\left(\phi+\tilde{\phi}^{(i,j)}(t)\right)}, \tag{2}$$

where P_0 is the common per-node transmit power, ϕ is the nominal beamforming phase and $\tilde{\phi}^{(i,j)}(t)$ is the phase error of the transmission from the i^{th} transmit node to the j^{th} receive node at prediction time $t > 0$ after the end of the measurement interval. If perfect coherence is achieved, then $\tilde{\phi}^{(i,j)}(t) = 0$ and $\overline{J}^{(j)}(t) = \mathbb{E}\left\{\left|\sum_{i=1}^{N_t} r^{(i,j)}(t)\right|^2\right\} = P_0\left(\sum_{i=1}^{N_t}|g_{i,j}|\right)^2$. In practice, however, the phase errors will not be zero due to channel estimation errors and the effect of stochastic clock drifts (as discussed in Section III). In fact, when the phase errors become large, the mean beamforming power is $\overline{J}^{(j)}(t) = P_0\sum_{i=1}^{N_t}|g_{i,j}|^2 = P_{\text{inc}}^{(j)}$, i.e., large phase errors result in incoherent average power.

To quantify the effect of nonzero phase errors on the steady-state beamforming power in the j^{th} slot, we assume $\tilde{\phi}^{(i,j)}(t)$ is a spatially independent and identically distributed (i.i.d.) zero mean Gaussian random process with variance $\sigma_\phi^2(\mu_j T_f, t)$ parameterized by the frame period T_f and the prediction interval t (this assumption will be justified in Section III). With this assumption, the mean beamforming power at prediction time t for the j^{th} receive node can be calculated as

$$\begin{aligned}\overline{J}^{(j)}(T_f,t) &= \mathbb{E}\left\{\left|\sum_{i=1}^{N_t} r^{(i,j)}(t)\right|^2\right\} \\ &= P_{\text{inc}}^{(j)}\left[1+(\rho_j-1)e^{-\sigma_\phi^2(\mu_j T_f,t)}\right],\end{aligned} \tag{3}$$

where $\rho_j = \frac{\left(\sum_{i=1}^{N_t}|g_{i,j}|\right)^2}{\sum_{i=1}^{N_t}|g_{i,j}|^2}$. When $\sigma_\phi^2(\mu_j T_f, t)$ is small, note that the mean beamforming power $\overline{J}^{(j)}(T_f,t) \approx P_{\text{inc}}^{(j)}\rho_j = P_0\left(\sum_{i=1}^{N_t}|g_{i,j}|\right)^2$ and the distributed array achieves approximately coherent power. Similarly, when $\sigma_\phi^2(\mu_j T_f, t)$ is large, $\overline{J}^{(j)}(T_f,t) \approx P_{\text{inc}}^{(j)}$ and the distributed array achieves approximately incoherent power. We can combine (3) with (1) to write

$$\begin{aligned}\overline{E}_b^{(j)} = \eta P_{\text{inc}}^{(j)}\Bigg[&(\rho_j-1)\int_{T_m}^{\mu_j T_f} e^{-\sigma_\phi^2(\mu_j T_f,t)}\,dt \\ &+(T_f - N_r T_m)\Bigg],\end{aligned} \tag{4}$$

where we use the fact that the steady-state beamforming power of each receive node is periodic with period T_f.

C. NWMEHR Maximization Problem

We are interested in maximizing the steady-state weighted sum rate of the net energy transferred to the receive nodes in the system. As a baseline, we can consider the scenario where the receive nodes simply harvest incoherent transmissions with no feedback. In this case, since the entire frame period is spent harvesting incoherent power, the weighted sum rate of the net energy transferred to the receive nodes in the system can be expressed as

$$\overline{C} = \eta\sum_{j=1}^{N_r}\gamma_j P_{\text{inc}}^{(j)} = \eta\sum_{j=1}^{N_r}\gamma_j P_0\sum_{i=1}^{N_t}\left|g_{i,j}\right|^2, \tag{5}$$

where γ_j is the energy harvesting weighting factor for receiver j. If the receive nodes provide channel state feedback to improve coherence, the net amount of energy harvested by the receive nodes in one frame is the amount of energy received via beamforming (and incoherent harvesting) minus the amount of energy used by the receiver for channel state feedback in that frame. We define NWMEHR as

$$\mathsf{NWMEHR} = \frac{1}{\overline{C}T_f}\sum_{j=1}^{N_r}\gamma_j\left(\overline{E}_b^{(j)} - E_r^{(j)}\right), \tag{6}$$

where $\overline{E}_b^{(j)}$ is from (1) and $E_r^{(j)}$ is the energy used by the j^{th} receive node for channel state feedback in one frame. Values of $\mathsf{NWMEHR} > 1$ correspond to scenarios where channel state feedback with DTB improves the efficiency of the WPT with respect to simple incoherent energy harvesting.

Using the results from the previous section, we can rewrite (6) as

$$\begin{aligned}\mathsf{NWMEHR} = 1 + \frac{1}{T_f}\Bigg(&\frac{\eta}{\overline{C}}\sum_{j=1}^{N_r}\gamma_j P_{\text{inc}}^{(j)}(\rho_j-1) \\ &\int_{T_m}^{\mu_j T_f} e^{-\sigma_\phi^2(\mu_j T_f,t)}\,dt - D\Bigg),\end{aligned} \tag{7}$$

with

$$D = N_r T_m + \frac{\sum_{j=1}^{N_r}\gamma_j E_r^{(j)}}{\overline{C}}, \tag{8}$$

where D corresponds to the total energy loss in one frame due to the measurement and the energy consumption for feedback.

The goal is to find the optimal frame period $T_f^\star$ (or, equivalently, optimal frame rate $1/T_f^\star$) to maximize the NWMEHR. Mathematically, we can formulate the problem as

Problem 1 (NWMEHR maximization problem).

$$\begin{aligned}\underset{T_f}{\text{maximize}} \quad & \mathsf{NWMEHR} \\ \text{subject to} \quad & T_f \in \left[\frac{T_m}{\mu_{\min}}, \infty\right)\end{aligned}$$

where $\mu_{\min} = \min\{\mu_1, \cdots, \mu_{N_r}\}$.

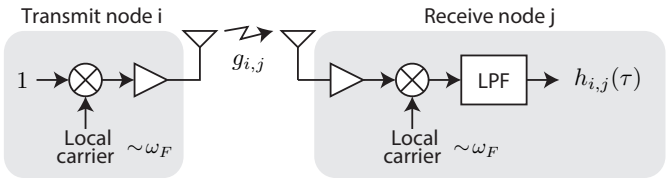

Fig. 3. Effective narrowband channel model including the effect of propagation, transmit and receive gains, and carrier offset.

In Section IV, we show that Problem 1 can sometimes be infeasible, i.e., there may be no solution in the feasible region $[T_m/\mu_{\min}, \infty)$ and, instead, the NWMEHR is maximized when the frame period $T_f = \infty$. This situation indicates that optimal strategy is for all the receive nodes to simply harvest incoherent power from the transmit nodes without any feedback.

III. FORWARD LINK CHANNEL TRACKING AND PREDICTION

The previous section established that the beamforming power (and resulting energy harvesting efficiency) is completely characterized by the variance $\sigma_\phi^2(T,t)$ of the phase error random process parameterized by the slot period T and the prediction interval t. In this section, we connect these statistics to the properties of the independent oscillators used by the transmit and receive nodes in the DTB system.

Fig. 3 shows the *effective* narrowband channel model from transmit node i to receive node j which includes the effects of propagation and carrier offset. Transmission from transmit node i to receive node j are conveyed on a carrier with nominal frequency ω_F, incur a phase shift of $\psi^{(i,j)} = \angle g_{i,j}$ over the wireless channel, and are then downmixed by receive node j using its local carrier nominally at ω_F. At time t, the effective narrowband channel from transmit node i to receive node j is modeled as

$$h_{i,j}(t) = g_{i,j} e^{j\left(\phi_t^{(i)}(t) - \phi_r^{(j)}(t)\right)} = |g_{i,j}| e^{j\phi^{(i,j)}(t)}, \qquad (9)$$

where $\phi_t^{(i)}(t)$ and $\phi_r^{(j)}(t)$ are the local carrier phase offsets at transmit node i and receive node j, respectively, at time t with respect to an ideal carrier reference, and $\phi^{(i,j)}(t) = \phi_t^{(i)}(t) - \phi_r^{(j)}(t) + \psi^{(i,j)}$ is the pairwise phase offset after propagation between transmit node i and receive node j at time t. In this paper, it is assumed that the channel magnitudes $|g_{i,j}|$ for $i = 1, \cdots, N_t$ and $j = 1, \cdots, N_r$ are fixed (or slowly varying) and perfectly known.

Each node in the system is assumed to have an independent local oscillator. These local oscillators behave stochastically, causing phase offset variations in each effective channel from each transmit node to the receive node. To characterize the oscillator dynamics of each node in the system, we consider a two-state model [39], [40] and define the state of the i^{th} transmit node's carrier as $\boldsymbol{x}_t^{(i)}(t) := [\phi_t^{(i)}(t), \omega_t^{(i)}(t)]^{\mathrm{T}}$, where $\phi_t^{(i)}(t)$ and $\omega_t^{(i)}(t)$ correspond to the carrier phase and frequency offsets in radians and radians per second at transmit node $i \in \{1, \cdots, N_t\}$ with respect to some reference carrier[3]. From [39], the dynamics of the i^{th} transmit node's carrier can be expressed as

$$\frac{d}{dt}\boldsymbol{x}_t^{(i)} = \begin{bmatrix} 0 & 1 \\ 0 & 0 \end{bmatrix} \boldsymbol{x}_t^{(i)} + \boldsymbol{u}_t^{(i)}(t), \qquad (10)$$

where $\boldsymbol{u}_t^{(i)}(t) \sim \mathcal{N}(0, \omega_F \cdot \mathrm{diag}(p,q))$ is the white Gaussian process noise vector parameterized by the nominal forward link carrier frequency ω_F and the white frequency noise and random walk frequency noise oscillator stability parameters p (units of seconds) and q (units of Hertz), respectively. We assume the process noise parameters to be identical at all nodes in the system. The receive nodes in the system also have independent local oscillators used to generate carriers for downmixing that are governed by the same dynamics as (10) with state $\boldsymbol{x}_r^{(j)}(t)$, process noise $\boldsymbol{u}_r^{(j)}(t)$ for $j = 1, \cdots, N_r$. We further define the *pairwise offset* state between the i^{th} transmit node and the j^{th} receive node after propagation as

$$\boldsymbol{\delta}^{(i,j)}(t) = \boldsymbol{x}_t^{(i)}(t) + \begin{bmatrix} \psi^{(i,j)} \\ 0 \end{bmatrix} - \boldsymbol{x}_r^{(j)}(t). \qquad (11)$$

For any sampling period T and sampling instances $t = nT$, standard methods can be used to write the discrete-time pairwise offset state update

$$\boldsymbol{\delta}^{(i,j)}[n+1] = \boldsymbol{F}(T)\boldsymbol{\delta}^{(i,j)}[n] + \boldsymbol{G}\boldsymbol{w}^{(i,j)}[n], \qquad (12)$$

where

$$\boldsymbol{F}(T) = \begin{bmatrix} 1 & T \\ 0 & 1 \end{bmatrix}, \quad \boldsymbol{G} = \begin{bmatrix} 1 & 0 & -1 & 0 \\ 0 & 1 & 0 & -1 \end{bmatrix}, \text{ and}$$
$$\boldsymbol{w}^{(i,j)}[n] = \begin{bmatrix} \boldsymbol{u}_t^{(i)}[n] \\ \boldsymbol{u}_r^{(j)}[n] \end{bmatrix}. \qquad (13)$$

The discrete-time process noise vectors $\boldsymbol{u}_t^{(i)}[n] \overset{\text{i.i.d.}}{\sim} \mathcal{N}(0, \boldsymbol{C}(T))$ and $\boldsymbol{u}_r^{(j)}[n] \overset{\text{i.i.d.}}{\sim} \mathcal{N}(0, \boldsymbol{C}(T))$ with

$$\boldsymbol{C}(T) = \omega_F^2 \begin{bmatrix} p + q\frac{T^3}{3} & q\frac{T^2}{2} \\ q\frac{T^2}{2} & qT \end{bmatrix}. \qquad (14)$$

Suppose the sampling period $T = T$ and that forward link channel measurements occur at $t = nT$ for $n = 0, 1, \cdots$. During the measurement intervals, we assume the pilot signals from each transmit node are short such that they only provide a useful estimate of the pairwise phase offset. Specifically, for the i^{th} transmit node's pilot at the j^{th} receive node in slot s, we assume an observation of the form

$$y^{(i,j)}[n] = \boldsymbol{h}\boldsymbol{\delta}^{(i,j)}[n] + v^{(i)}[n], \qquad (15)$$

where $\boldsymbol{h} = [1, 0]$ and $v^{(i)}[k] \overset{\text{i.i.d.}}{\sim} \mathcal{N}(0, R)$ is the measurement noise which is assumed to be spatially and temporally i.i.d. These observations facilitate tracking and prediction of the pairwise offset states at the receive nodes. We assume receive node j implements a bank of N_t separate two-state Kalman filters to track and predict the states $\boldsymbol{\delta}^{(i,j)}[n]$ for all $i = 1, \cdots, N_t$. When receive node j provides feedback to the

[3] Although the focus here is on a two-state model, the approach described here can also be applied to higher order oscillator models, e.g., [41], [42], with some additional notational and computational complexity.

transmit cluster after the n^{th} measurement, it transmits the most recent Kalman filter estimates $\hat{\boldsymbol{\delta}}^{(i,j)}[n\,|\,n]$ for all $i = 1, \cdots, N_t$. The transmit nodes use these estimates to generate predictions $\hat{\boldsymbol{\delta}}^{(i,j)}[n+t\,|\,n] = \boldsymbol{F}(t)\hat{\boldsymbol{\delta}}^{(i,j)}[n\,|\,n]$ for $t > 0$ in the subsequent beamforming interval to receive node j. Note that t is a continuous parameter and $\boldsymbol{F}(t)$ is defined for all $t > 0$.

It can be shown that the system described in (12) and (15) is completely observable and completely controllable, hence the Kalman filter steady-state prediction covariance

$$\boldsymbol{P}(T) = \begin{bmatrix} P_1(T) & P_2(T) \\ P_2(T) & P_3(T) \end{bmatrix} \in \mathbb{R}^{2\times 2}, \tag{16}$$

is the unique positive definite solution of the discrete-time algebraic Riccati equation (DARE) [43]

$$\boldsymbol{P}(T) = \boldsymbol{F}(T)\left[\boldsymbol{P}(T) - \frac{\boldsymbol{P}(T)\boldsymbol{h}^{\mathrm{T}}\boldsymbol{h}\boldsymbol{P}(T)}{\boldsymbol{h}\boldsymbol{P}(T)\boldsymbol{h}^{\mathrm{T}} + R}\right]\boldsymbol{F}^{\mathrm{T}}(T) + \boldsymbol{Q}(T), \tag{17}$$

where

$$\begin{aligned} \boldsymbol{Q}(t) = \boldsymbol{G}\mathrm{cov}\left\{\boldsymbol{w}^{(i,j)}[k]\right\}\boldsymbol{G}^{\mathrm{T}} &= \begin{bmatrix} At + \frac{B}{3}t^3 & \frac{B}{2}t^2 \\ \frac{B}{2}t^2 & Bt \end{bmatrix} \\ &= \begin{bmatrix} Q_1(t) & Q_2(t) \\ Q_2(t) & Q_3(t) \end{bmatrix}, \end{aligned} \tag{18}$$

with $A = 2\omega_F^2 p$ and $B = 2\omega_F^2 q$. Note that $\boldsymbol{P}(T) \succ \boldsymbol{0}$ corresponds to the covariance matrix of the steady-state Kalman filter predictions just prior to a measurement/observation. The Kalman filter steady-state *estimation* covariance immediately after receiving an observation can be expressed as

$$\boldsymbol{S}(T) = \begin{bmatrix} S_1(T) & S_2(T) \\ S_2(T) & S_3(T) \end{bmatrix} = \boldsymbol{P}(T) - \frac{\boldsymbol{P}(T)\boldsymbol{h}^{\mathrm{T}}\boldsymbol{h}\boldsymbol{P}(T)}{\boldsymbol{h}\boldsymbol{P}(T)\boldsymbol{h}^{\mathrm{T}} + R}. \tag{19}$$

We denote $\hat{\boldsymbol{S}}(T,t) = \boldsymbol{F}(t)\boldsymbol{S}(T)\boldsymbol{F}^{\mathrm{T}}(t)$ and note that the (1,1) element of this matrix can be written as

$$\hat{S}_1(T,t) = S_1(T) + 2tS_2(T) + t^2 S_3(T). \tag{20}$$

Moreover, since the steady-state prediction covariance at any prediction time $t > 0$ after an observation, i.e., after the commencement of beamforming, can be written as $\hat{\boldsymbol{P}}(T,t) = \hat{\boldsymbol{S}}(T,t) + \boldsymbol{Q}(t)$, we have

$$\begin{aligned} &\hat{P}_1(T,t) \\ &= \hat{S}_1(T,t) + Q_1(t) \\ &= S_1(T) + 2tS_2(T) + t^2 S_3(T) + \omega_F^2 t\left(p + q\frac{t^2}{3}\right). \end{aligned} \tag{21}$$

Note that $\hat{P}_1(T,t)$ is the (1,1) element of the Kalman filter's prediction covariance at prediction time $t > 0$ after an observation. This quantity corresponds to the steady-state *phase prediction variance* of the Kalman filter. Since this quantity fully characterizes the steady-state expected beamforming gain of the transmit array, we denote $\sigma_\phi^2(T,t) = \hat{P}_1(T,t)$.

Recall that in Section II, we obtain the expression of NWMEHR in terms of $\sigma_\phi^2(\mu_j T_f, t)$ for $j = 1, \cdots, N_r$. In this section, we have shown that $\sigma_\phi^2(\mu_j T_f, t)$ for any j is an implicit function with respect to T_f. Therefore, combining these two results, we finally obtain an implicit function of NWMEHR only in terms of the frame period T_f. In the next section, we develop a numerical method to find the optimal frame period to maximize the NWMEHR.

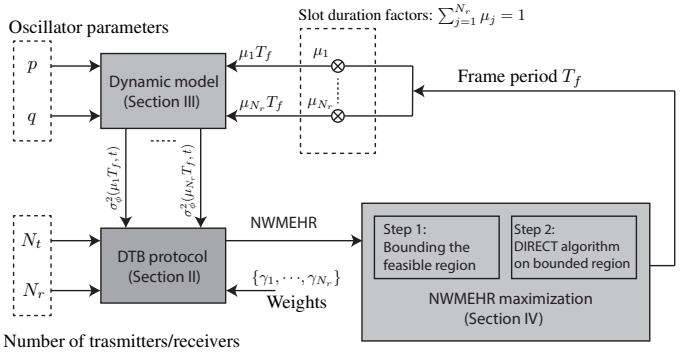

Fig. 4. Overview of the NWMEHR maximization problem.

IV. ANALYSIS

This section analyzes Problem 1 and develops a method to numerically compute the globally optimal frame period T_f to maximize the NWMEHR. An overview of the modeling and optimization methodology is shown in Fig. 4. We assume all of the process and measurement noise parameters are known by the receive nodes. If these parameters are unknown, covariance estimation techniques such as [44], can be used to estimate these parameters as part of the Kalman filtering process. We also assume the slot duration factors are given, perhaps determined by a separate process aware of the charging state of each receiver. Given a frame period T_f, the NWMEHR can be calculated from (6). To find the globally optimum value of T_f, the main steps we will follow in this section are (i) bounding the feasible region and (ii) applying the direct algorithm on the bounded region.

First, some basic properties of Problem 1 are summarized below:

(1) The objective function of Problem 1 is only a function of one variable: the frame period T_f.
(2) The objective function of Problem 1 is nonlinear and nonconvex.
(3) The objective function of Problem 1 is implicit since it requires solving the DARE in (17), which, in general, has no closed-form explicit solution.
(4) Problem 1 has one simple linear inequality constraint and the feasible region of Problem 1 is unbounded.

We will first address the problem of the unbounded feasible region in the following section. In the process of bounding the feasible region, we can also check a necessary condition for the existence of a finite solution to Problem 1.

A. Bounding the Feasible Region

In this section, we develop an efficient method to bound the feasible region for Problem 1 into a *closed* interval. To facilitate the analysis, the following lemma describes some basic properties of the NWMEHR function defined in (7).

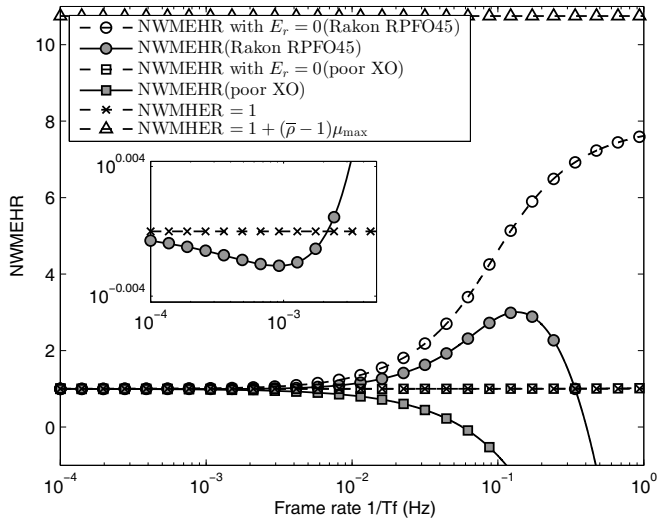

Fig. 5. Two examples of the NWMEHR and the NWMEHR with $E_r = 0$ versus the frame rate $1/T_f$.

Lemma 1. *The NWMEHR defined in (7) has the following properties:*

$$\lim_{T_f \to \infty} \mathsf{NWMEHR} = 1 \textit{ from below, and}$$

$$\sup_{T_f \in \left[\frac{T_m}{\mu_{\min}}, \infty\right)} \mathsf{NWMEHR} \in [1, 1 + (\overline{\rho} - 1)\mu_{\max}),$$

where

$$\overline{\rho} = \frac{\sum_{j=1}^{N_r} \gamma_j P_{\text{inc}}^{(j)} \rho_j}{\sum_{j=1}^{N_r} \gamma_j P_{\text{inc}}^{(j)}}, \textit{ and} \tag{22}$$

$$\mu_{\max} = \max\{\mu_1, \cdots, \mu_{N_r}\}. \tag{23}$$

Proof. Please refer Appendix -A. □

To illustrate these properties, Fig. 5 shows examples of the NWMEHR and the NWMEHR with $E_r = 0$ for systems with two different oscillator parameters from Table 1 based on the "Rakon RPFO45" [45] and the "poor XO" [46], respectively. For this example, we assume $N_t = 15$ transmit nodes and $N_r = 2$ receive nodes and weights $\gamma = \{1, 1\}$ and slot duration factors $\mu = \{0.3, 0.7\}$. For both the poor XO and the Rakon RPFO45, the NWMEHR with $E_r = 0$ increases with the slot rate as expected. The NWMEHR after accounting for the cost of feedback, however, is monotonically decreasing for the system with the poor XO. In this case, since $\mathsf{NWMEHR} < 1$ for all $T_f \in [T_m/\mu_{\min}, \infty)$, the NWMEHR is maximized when the receive nodes provide no feedback ($1/T_f = 0$) and simply harvest incoherent power from the transmit nodes. For Rakon RPFO45, we observe the NWMEHR deceases rapidly when $1/T_f$ is large and achieves its global maxima of $\mathsf{NWMEHR} \approx 3.0$ at $1/T_f \approx 0.14$ Hz. In this case, the receiver achieves the maximum energy harvesting rate by providing periodic feedback to the transmit nodes. The zoomed inset in Fig. 5 also shows the NWMEHR converging to 1 from below as $T_f \to \infty$ for Rakon RPFO45.

Since we are interested in slot periods that result in energy harvesting rates that exceed incoherent energy harvesting, we can define the set

$$\mathcal{X}_{\mathsf{NWMEHR}} = \left\{ T_f \geq \frac{T_m}{\mu_{\min}} : \mathsf{NWMEHR} \geq 1 \right\}. \tag{24}$$

An important consequence of Lemma 1 is that $\mathcal{X}_{\mathsf{NWMEHR}}$ must be bounded or empty. Due to the implicit nature of the NWMEHR function, however, finding the exact bounds on this set can be difficult. To facilitate analysis, we propose a function $\Phi(T_f)$ which is an upper bound for the NWMEHR for all $T_f \geq T_m/\mu_{\min}$. Hence, the set $\mathcal{X}_\Phi = \{T_f \geq T_m/\mu_{\min} : \Phi(T_f) \geq 1\}$ is a superset of $\mathcal{X}_{\mathsf{NWMEHR}}$, i.e., $\mathcal{X}_{\mathsf{NWMEHR}} \subseteq \mathcal{X}_\Phi$. If $\mathcal{X}_{\mathsf{NWMEHR}}$ is nonempty, then it and $\mathcal{X}_\Phi$ must contain the value of T_f resulting in the globally optimal NWMEHR, which is the solution of Problem 1. Conversely, if $\mathcal{X}_\Phi$ is empty, then $\mathcal{X}_{\mathsf{NWMEHR}}$ is also empty and the optimal strategy is to set $T_f = \infty$ to simply harvest incoherent energy without feedback.

To develop the NWMEHR upper bound $\Phi(T_f)$, we first provide the following Lemma.

Lemma 2. *For all $T \geq T_m$ and all $t > 0$, the $(1,1)$ element of the matrix $\hat{\boldsymbol{S}}(T,t) = \boldsymbol{F}(t)\boldsymbol{S}(T)\boldsymbol{F}^{\mathrm{T}}(t)$ is lower bounded as*

$$\hat{S}_1(T,t) \geq \hat{S}_1^{(0)}(T,t) = t^2 \sqrt{AB + \frac{B^2}{12} T^2}, \tag{25}$$

where $A = 2\omega_F^2 p$ and $B = 2\omega_F^2 q$.

Proof. Please refer to Appendix -B. □

Recall that the mean beamforming power $\overline{J}(T,t)$ is related to $\hat{S}_1(T,t)$ through (21) and (3). By providing an explicit lower bound on $\hat{S}_1(T,t)$ (which does not require solving a DARE), we also have a lower bound on the phase variance $\sigma_\phi^2(T,t) = \hat{S}_1(T,t) + Q_1(t)$, and hence an upper bound on $\overline{J}(T,t)$. From this result, we can obtain a simple closed-form and explicit upper bound $\Phi(T_f)$ for the NWMEHR for all $T_f \geq T_m/\mu_{\min}$. The result is summarized in Proposition 1.

Proposition 1. *Define*

$$\beta = \sqrt{\int_0^\infty e^{-2Q_1(t)}\, dt} > 0, \tag{26}$$

where $Q_1(t)$ is the $(1,1)$ element of the process noise covariance matrix $\boldsymbol{Q}(t)$. For all $T_f \geq T_m/\mu_{\min}$, we have

$$\begin{aligned} \Phi(T_f) &= 1 + \frac{1}{T_f}\left(\frac{\beta\eta}{\overline{C}} \sum_{j=1}^{N_r} \gamma_j P_{\text{inc}}^{(j)} (\rho_j - 1) \Lambda(\mu_j T_f) - D \right) \\ &\geq \mathsf{NWMEHR}, \end{aligned} \tag{27}$$

with

$$\Lambda(\mu_j T_f) = \frac{1}{\left(\frac{8}{\pi} \hat{S}_1^{(0)}(\mu_j T_f, 1)\right)^{\frac{1}{4}}}, \tag{28}$$

where D are defined in (8), respectively.

Proof. Please refer to Appendix -C. □

Note that $\Phi(T_f)$ shares the property with the NWMEHR that $\lim_{T_f \to \infty} \Phi(T_f) = 1$ from below. To see why this is the case in

general, note that $\Lambda(\mu_j T_f)$ is a monotonically decreasing function with respect to T_f since $\hat{S}_1^{(0)}(\mu_j T_f, 1)$ is monotonically increasing and $\Phi(T_f)$ is a linear combination of $\Lambda(\mu_j T_f)$ for $j = 1, \cdots, N_r$. Since $\beta > 0$ and $D > 0$, it follows that, for all T_f larger than a threshold T_{ub},

$$\frac{\beta\eta}{\overline{C}} \sum_{j=1}^{N_r} \gamma_j P_{\text{inc}}^{(j)} (\rho_j - 1) \Lambda(\mu_j T_f) < D.$$

Hence, as $T_f \to \infty$, we have $\Phi(T_f) \to 1$ from below.

This result implies that $\mathcal{X}_\Phi$ is either an empty set or a closed bounded interval $[T_m/\mu_{\min}, T_{ub}]$, where T_{ub} is the solution to

$$\sum_{j=1}^{N_r} \gamma_j P_{\text{inc}}^{(j)} (\rho_j - 1) \Lambda(\mu_j T_{ub}) = \frac{\overline{C} D}{\beta\eta}. \tag{29}$$

Note that (29) is a one-dimensional equation with respect to T_{ub}, which can be solved easily using any root-finding algorithm like the Brent's method [47]. If no value of $T_{ub} > T_m/\mu_{\min}$ is found, then the optimal strategy is to provide no feedback and to simply harvest incoherent energy. In the following section, we assume $T_{ub} > T_m/\mu_{\min}$ such that $\mathcal{X}_\Phi = [T_m/\mu_{\min}, T_{ub}] \neq \emptyset$ is a bounded interval and develop a method to search the maximum NWMEHR over $\mathcal{X}_\Phi$.

B. Maximizing the NWMEHR on the Bounded Search Region

Based on the analysis in the prior section, we assume in this section that we have a closed bounded nonempty interval $\mathcal{X}_\Phi = [T_m/\mu_{\min}, T_{ub}]$ for the feasible region of Problem 1. This section describes a method for finding the value of $T_f \in \mathcal{X}_\Phi$ that maximizes the NWMEHR. Since the NWMEHR is an implicit function of T and requires solving a DARE, we rely on numerical methods to efficiently find the optimal solutions.

As a technical detail, recall that $\mathcal{X}_{\mathsf{NWMEHR}} \subseteq \mathcal{X}_\Phi$. If both $\mathcal{X}_{\mathsf{NWMEHR}}$ and $\mathcal{X}_\Phi$ are non-empty, then the procedure described below will find the globally optimal value of T_f which maximizes the NWMEHR. It is possible, however, that $\mathcal{X}_{\mathsf{NWMEHR}}$ is empty even when $\mathcal{X}_\Phi$ is nonempty. When this occurs, the procedure described below will still return the value of $T_f \in \mathcal{X}_\Phi$ that maximizes the NWMEHR, but the resulting NWMEHR will be less than one. If this occurs, we set $T_f = \infty$, which corresponds to no feedback and only incoherent power is harvested, to maximize the NWMEHR.

There are several potential numerical methods that can be used to solve one-dimensional optimization problems over closed bounded intervals. Most one-dimensional search algorithms, such as line search, golden section search, or parabolic interpolation (Brent's method) [48], can only guarantee convergence to locally optimal solutions. Hence, a prerequisite of applying those algorithms is to show that the NWMEHR can not have more than one local maximum in $\mathcal{X}_\Phi$. This is difficult to show, however, since the objective function of Problem 1 is governed by the DARE in (17), which, in general, has no closed-form and explicit expression.

Another approach to solving one-dimensional optimization problems like Problem 1 is to use the DIRECT algorithm [38]. The DIRECT optimization algorithm solves a class of *global* optimization problems over closed bounded intervals. The DIRECT algorithm is especially suitable for solving Problem 1 for the following reasons:

(1) The DIRECT algorithm does not require the knowledge of the gradient of the objective function. Since the objective function of Problem 1 is implicit (requiring a solution of the DARE in (17)) and has no closed-form, it is not straightforward to obtain the gradient of the objective function.
(2) Given a bounded domain, the DIRECT algorithm *globally* converges to the maximal value of the objective function, even in the presence of local maxima.

Application of the DIRECT algorithm requires (i) a bounded search region and (ii) the objective function is continuous or at least continuous in the neighborhood of a global optimum [38]. In Section IV-A, we bounded the search region of the optimal slot period by $\mathcal{X}_\Phi$. The following proposition establishes that the NWMEHR is a continuous function of T_f on the domain $[T_m/\mu_{\min}, \infty)$ and thus, on $\mathcal{X}_\Phi \subseteq [T_m/\mu_{\min}, \infty)$.

Proposition 2. *The NWMEHR defined in (7) is a continuous function with respect to the frame period T_f on the domain $[T_m/\mu_{\min}, \infty)$.*

Proof. Please refer to Appendix -D. □

In light of Proposition 2, we can apply the DIRECT algorithm straightforwardly on the closed bounded domain $\mathcal{X}_\Phi$. In each iteration, the DIRECT algorithm partitions the search interval into finer sub-intervals by identifying the potentially optimal intervals using a rate-of-change constant, which indicates how much emphasis to place on global versus local search. Once the global part of the algorithm finds the basin of convergence of the optimum, the local part of the algorithm quickly and automatically exploits it [38]. Note that the complexity of the whole procedure is dominated by step 2 since the time required to solve the one-dimensional equation in step 1 is insignificant compared to the time required to solve the iterative DIRECT algorithm in step 2. As mentioned in [38] with regards to the number of iterations for DIRECT, "When a Lipschitz constant is not known, the algorithm stops after a prespecified number of iterations". Hence, in step 2, we use a fixed number of iterations N_i to be the stopping criteria. In each iteration, the maximum number of function evaluations is N_f. For each function evaluation, we need to solve N_d 2×2 DAREs. In general, there would be $N_d = N_t N_r$ 2×2 DAREs to solve in our system. When the oscillator parameters are identical at all of the transmit nodes, it is actually only necessary to solve $N_d = N_r$ 2×2 DAREs due to the common parameters. Thus, in each function evaluation, we need to solve the DARE in (17) N_r times by setting $T = \mu_j T_f$ to obtain $\sigma_\phi^2(\mu_j T_f, t)$ for $j = 1, \cdots, N_r$. Each DARE has the same complexity. Therefore, the complexity of the whole procedure scales as $N_i N_f N_t N_r$ or $N_i N_f N_r$ times of the complexity of solving a single 2×2 DARE when the transmit nodes have differing or identical oscillator parameters, respectively.

The following section presents numerical results based on the NWMEHR-maximizing search strategies developed in this section. The results show that the optimal slot period can be found successfully and efficiently using the proposed algorithms.

V. NUMERICAL RESULTS

This section provides numerical results to verify the optimization method described in the previous section and demonstrate the potential of DTB for WPT with practical system parameters. We assume a feedback-based system with frequency division duplexed (FDD) forward and reverse links on separate frequencies. Table 1 lists the parameters of the oscillators and other general parameters for both forward and reverse links, where OSS and OLS denote "oscillator short-term stability" and "oscillator long-term stability" parameters, respectively. The process noise parameters p and q in Table 1 are chosen based on typical inexpensive crystal oscillator parameters [46] and Rakon RFPO45 oven-controlled oscillator datasheet [45]. Tables 2 and 3 list the particular parameters for forward and reverse links, respectively. To apply the DIRECT algorithm, we set the total number of iterations N_i to be $1,000$ and the maximum number of function evaluations N_f to be $1,000$ in all our simulations.

While our analysis is general with respect to the receive node energy consumption model, we assume the model from [49] in the numerical results presented in this section. Specifically, the feedback energy used by the j^{th} receive node in a frame is modeled as

$$E_r^{(j)} = \left[\frac{\zeta}{\mu} P_t^{(j)} + P_c\right] T_{on} + P_{tr} T_{tr}, \tag{30}$$

where μ is the drain efficiency of the RF amplifier, ζ is the Peak to Average Ratio, $P_t^{(j)}$ is the power for feedback transmission, P_c and P_{tr} are the power consumptions of the transmitter circuitry on active and transient mode, respectively, and T_{on} and T_{tr} are the durations of the transmitter circuitry on active and transient mode, respectively. To ensure that the transmit nodes can correctly decode the feedback from receive node j, the transmit power $P_t^{(j)}$ for sending feedback is assumed to be fixed and larger than a minimum decoding threshold $P_{\text{dec}}^{(j)}$. Since the durations of the transmitter circuitry on active and transient mode are much smaller than that of measurement, i.e., $T_{on} \ll T_m$ and $T_{tr} \ll T_m$, we are assuming the feedback to be instantaneous. The power consumption of transmitter circuitry P_c is calculated according to [49], which includes the power consumptions of the mixer, the frequency synthesizer, the digital-to-analog converter and the filters. Fig. 6 shows the geometry of the network. Both the transmit and receive nodes are equidistantly placed on lines with length 5 meters. Thus, the distance d_{ij} between the i^{th} transmit node and j^{th} receive node can be calculated as $d_{ij} = 10\sqrt{1 + (i/(N_t+1) - j/(N_r+1))^2}$ meters for $i = 1, \cdots, N_t$ and $j = 1, \cdots, N_r$. The weights are assumed to be unit for all receive nodes, i.e., $\gamma_j = 1$ for $j = 1, \cdots, N_r$.

Using a link-budget analysis as in [32], we first calculate the minimum decoding threshold. Assuming a thermal noise floor of -174 dBm, we can calculate the power of the additive white Gaussian noise at each transmit node as $-174 + 10\log_{10} B_R = -104$ dBm. We assume the transmitters require 3dB SNR to decode the feedback. Hence, the received signal power at each transmit node should be at least $-104 + 3 = -101$ dBm. The reverse link path loss from the j^{th} receive node to the i^{th} transmit node can be calculated as $10\log_{10}\left(\frac{4\pi d_{ij}\omega_R}{2\pi c}\right)^{\alpha} = 60.07 + 30\log_{10}(d_{ij})$ dB, where $c = 3 \times 10^8$ m/sec is the velocity of light. Thus, the minimum transmit power for the j^{th} receive node sending feedback to the i^{th} transmit node should be $-101 + 60.07 + 30\log_{10}(d_{ij}) - G_r = -40.93 + 30\log_{10}(d_{ij})$ dBm or $8.07 \times 10^{-8}(d_{ij})^3$ Watts. Thus, the minimum transmit power for the j^{th} receive node sending feedback is then $P_{\text{dec}}^{(j)} = 8.07 \times 10^{-8}(\max_i\{d_{ij}\})^3$ Watts. Since $d_{ij} \leq 10\sqrt{2}$ for all i and j, we assume the transmit power for the j^{th} receive node sending feedback is $P_t^{(j)} = 8.07 \times 10^{-8} \cdot (10\sqrt{2})^3 = 2.28 \times 10^{-4}$ Watts. The time to send feedback to one transmit node is $\frac{L}{R_R} = 5.33 \times 10^{-6}$ sec. Hence, the total time to send feedback to all transmit nodes, which is also the duration of the transmitter circuitry on active mode, is $T_{on} = N_t \cdot 5.33 \times 10^{-6}$ sec. Based on (30), The total energy for

Table 1. General parameters.

Case	Parameter	Value	Units	Meaning
Good XO	p	2.48×10^{-24}	sec	OSS
	q	7.44×10^{-27}	Hertz	OLS
Poor XO	p	6.34×10^{-18}	sec	OSS
	q	2.57×10^{-23}	Hertz	OLS
Rakon RPFO45	p	2.31×10^{-21}	sec	OSS
	q	6.80×10^{-23}	Hertz	OLS
	α	3		Path loss exponent
	η	0.70		Energy harvesting efficiency

Table 2. Parameters for forward link.

Parameter	Value	Units	Meaning
ω_F	$2\pi \times 10^9$	rad/sec	Carrier frequency
T_0	50×10^{-6}	sec	Duration of measurement for single transmitter
P_0	1	Watts	Transmit power per node
L	32		Number of bits per channel measurement
G_t	6	dBi	Transmitter's antenna gains
R	5×10^{-10}	rad^2	Measurement noise

Table 3. Parameters for reverse link.

Parameter	Value	Units	Meaning
ω_R	$4.8\pi \times 10^9$	rad/sec	Carrier frequency
B_R	10×10^6	Hertz	Reverse link bandwidth
R_R	6	Mbps	Reverse link data rate
G_r	0	dBi	Receiver's antenna gains
P_c	0.1	Watts	Circuitry power on active mode
P_{tr}	0.05	Watts	Circuitry power on transient mode
T_{tr}	5×10^{-6}	sec	Duration on transient mode
ζ	10	dB	Peak to average ratio
μ	0.35		Drain efficiency of RF amplifier

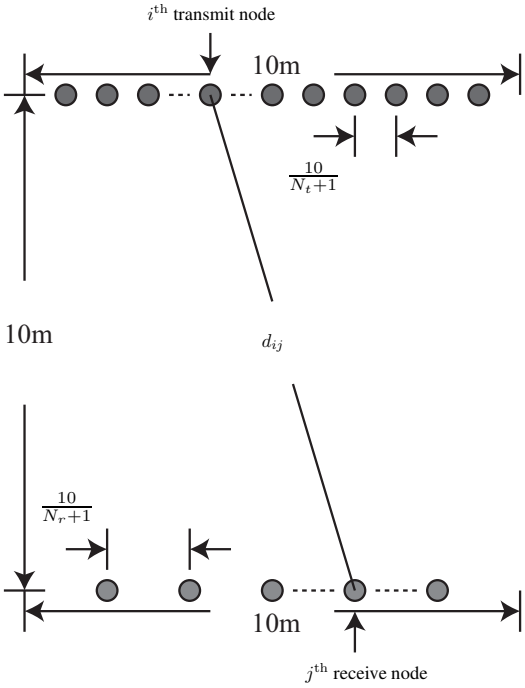

Fig. 6. Geometry of the network.

feedback from the j^{th} receive node to N_t transmit nodes is

$$E_r^{(j)} = \left(\frac{\zeta}{\mu}P_t^{(j)} + P_c\right)T_{on} + P_{tr}T_{tr}$$
$$= (N_t \cdot 5.68 + 2.50) \times 10^{-7} \text{ Joules.}$$

To obtain the forward link path loss from the receive nodes to the i^{th} transmit node, we use the forward link carrier frequency ω_F to calculate $|g_{i,j}|^2 = \left(\frac{4\pi d_{ij}\omega_F}{2\pi c}\right)^{-\alpha} \cdot 10^{\frac{G_t}{10}} = 5.42 \times 10^{-5}\,(d_{ij})^{-3}$ for $i = 1, \cdots, N_t$ and $j = 1, \cdots, N_r$.

Fig. 7 shows the optimal frame rate (in Hertz) and the maximum NMEHR versus oscillator parameters p and q for small network ($N_t = 15$ and $N_r = 2$) and large network ($N_t = 100$ and $N_r = 50$), respectively. The slot duration factor for each receive node is randomly selected from $(0, 1)$ and normalized to make the summation to be one. It is observed that the optimal frame rate increases when either oscillator parameter p or oscillator parameter q increases. Since in order to achieve the maximum NWMEHR, the system requires the channel information more frequently to compensate for the bad channel estimation caused by the poor oscillator parameters. In all four subplots, we also show dark blue regions in where no feedback is needed. In these areas, the system has low-quality oscillators and thus, the increment of the beamforming power by increasing the frame rate can not compensate for the increment of the energy used for feedback.

Fig. 8 shows the optimal frame rate and the maximum WMEHR versus the numbers of transmit nodes N_t and receive nodes N_r. The WMEHR denotes the weighted mean energy harvested rate, i.e., $\mathsf{WMEHR} = \overline{C} \cdot \mathsf{NWMEHR}$. The slot duration factor for each receive node is equal to be $1/N_r$. It is observed that when N_r is fixed, the optimal frame rate increases when N_t increases. This is caused by the fact that the energy consumption

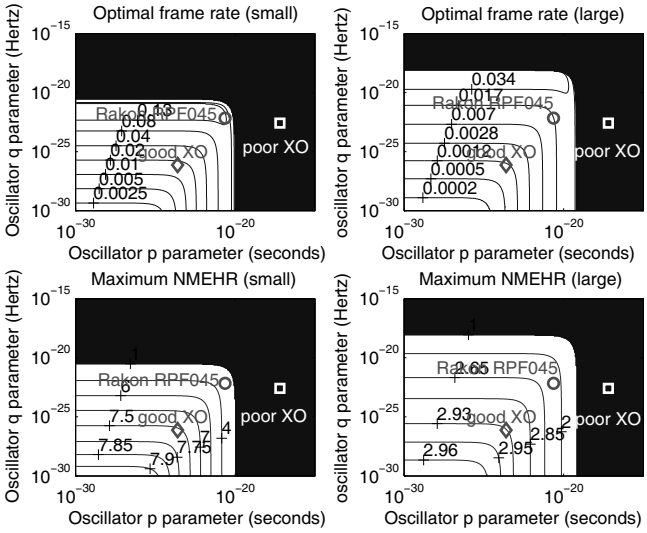

Fig. 7. Optimal frame rate (in Hertz) and maximum NWMEHR versus oscillator parameters p and q for small network ($N_t = 15$ and $N_r = 2$) and large network ($N_t = 100$ and $N_r = 50$). The shaded region corresponds to conditions under which the optimal strategy is to set the optimal slot rate to zero and harvest incoherent energy.

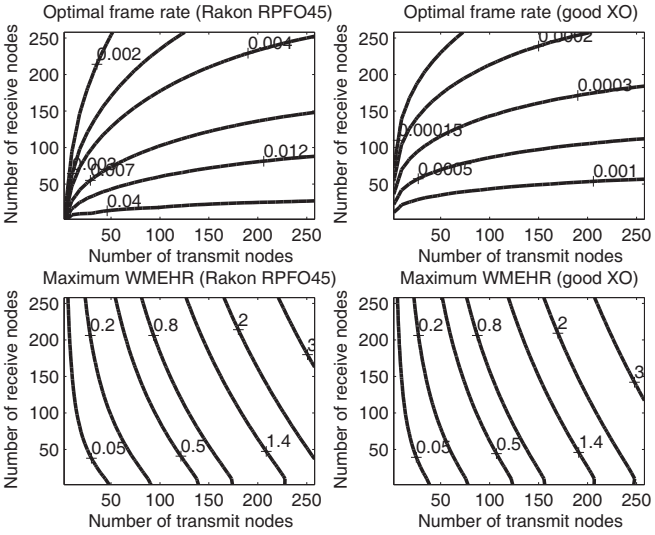

Fig. 8. Optimal frame rate (in Hertz) and the maximum WMEHR (in milliWatts) versus numbers of transmit nodes N_t and receive nodes N_r.

for feedback increases linearly with respect to N_t and thus the receive nodes have to provide more frequent feedback. It is also observed that when N_t is fixed and small ($N_t < 50$), the optimal frame rate is insensitive to N_r and when N_t is large ($N_t > 100$), the optimal frame rate decreases when N_r increases.

VI. CONCLUSIONS AND FUTURE WORK

This paper considers the problem of improving the efficiency of wireless power transfer over distance through distributed transmit beamforming. By using a distributed array, the system can achieve good directivity without the use of a large, expensive conventional array. Our system model accounts for the energy of feedback for feedback-based beamforming systems. An

optimization problem is formulated to find the optimal feedback period (or feedback rate) to maximize the net energy harvesting rate when local oscillators of the transmit nodes and receive node experience stochastic dynamics. We provide a numerical method to solve the problem by first bounding the search region according to an upper bound function of the NWMEHR and then applying the DIRECT algorithm on that region. Numerical results verify the analysis and demonstrate the potential for using distributed transmit beamforming in wireless power transfer systems.

In this paper, our focus was on a time slotted DTB protocol where the transmit array steers a beam toward one intended receive node at a time. While the "unintended" receivers still harvest incoherent energy during this time, such an approach may be suboptimal with respect to a DTB protocol where the transmit phases are optimized for simultaneous semi-coherent beamforming to multiple receivers over the full duration of each frame. We note that the NWMEHR framework developed in this paper can be extended to this scenario by jointly optimizing a N_t+1 dimensional variable containing the transmit phases and feedback rate. Since each transmit phase is naturally bounded on any interval of length 2π, we can use a similar approach as in Section IV to bound the feedback period and hence bound the N_t+1 dimensional optimization variable. Since the new N_t+1 variable is bounded and the objective function is continuous, we can then apply the DIRECT algorithm to find the optimal solution.

APPENDICES

A. Proof of Lemma 1

To show the NWMEHR converges to 1 from below when $T_f \to \infty$, we show $\int_{T_m}^{T} e^{-\sigma_\phi^2(T,t)}\,dt \to 0$ when $T \to \infty$. From (21), we have

$$\int_{T_m}^{T} e^{-\sigma_\phi^2(T,t)}\,dt \le \sqrt{\int_0^\infty e^{-2\hat{S}_1(T,t)}\,dt} \times \sqrt{\int_0^\infty e^{-2Q_1(t)}\,dt}, \tag{31}$$

where the equality comes from the Cauchy-Schwarz inequality and results from the nonnegativity of $e^{-2\hat{S}_1(T,t)}$ and $e^{-2Q_1(t)}$ and $[T_m, T] \subseteq [0,\infty)$. Since $\sqrt{\int_0^\infty e^{-2Q_1(t)}\,dt}$ is bounded, thus, it suffices to show $\lim_{T\to\infty}\int_0^\infty e^{-2\hat{S}_1(T,t)}\,dt = 0$. According to (20), it follows

$$\lim_{T\to\infty}\int_0^\infty e^{-2\hat{S}_1(T,t)}\,dt \le \lim_{T\to\infty}\int_0^1 e^{-t^2 S_3(T)}\,dt + \lim_{T\to\infty}\int_1^\infty e^{-t^2 S_3(T)}\,dt, \tag{32}$$

where the equality results from the nonnegativity of $S_1(T)$, $tS_2(T)$ for any $T \in [T_m,\infty)$ and $t \ge 0$. For the first term of the right-hand side (RHS) of (32), it follows $\lim_{T\to\infty}\int_0^1 e^{-t^2 S_3(T)}\,dt = \int_0^1 \lim_{T\to\infty} e^{-t^2 S_3(T)}\,dt = 0$ from the Lebesgue's dominated convergence theorem and $\lim_{T\to\infty} S_3(T) = \infty$ since $S_3(T)$ is the Kalman filter steady-state estimation variance of the frequency. For the second term of the RHS of (32), it follows $\lim_{T\to\infty}\int_1^\infty e^{-t^2 S_3(T)}\,dt \overset{(a)}{\le} \lim_{T\to\infty}\frac{1}{S_3(T)}e^{-S_3(T)} \overset{(b)}{=} 0$, where (a) results from $e^{-t^2 S_3(T)} \le e^{-tS_3(T)}$ for all $t \in [1,\infty)$ with fixed T and (b) comes from the fact $\lim_{T\to\infty} S_3(T) = \infty$.

If the NWMEHR attains its maximum at infinity, then we know $\sup_{T_f\in[T_m/\mu_{\min},\infty)} \mathsf{NWMEHR} = 1$ from prior analysis. Otherwise, the NWMEHR attains its maximum in the interval $(T_m/\mu_{\min},\infty)$, which implies $\sup_{T_f\in[T_m/\mu_{\min},\infty)} \mathsf{NWMEHR} \ge 1$. Hence, $\sup_{T_f\in[T_m/\mu_{\min},\infty)} \mathsf{NWMEHR} \ge 1$. On the other hand, if we denote $\mu_{\max} = \max\{\mu_1,\cdots,\mu_{N_r}\}$, from (7), it follows $\mathsf{NWMEHR} \le 1 + \frac{\eta}{C}\sum_{j=1}^{N_r}\gamma_j P_{\text{inc}}^{(j)}(\rho_j - 1)\mu_{\max} = 1 + (\overline{\rho}-1)\mu_{\max}$, where $\overline{\rho}$ is defined in (22). This completes the proof of Lemma 1.

B. Proof of Lemma 2

The proof mainly involves two steps. **Step 1** shows $\hat{S}_1(T,t)$ is a monotonically increasing function of $R \in (0,\infty)$ for fixed $T \ge T_m$ and $t > 0$. **Step 2** shows that $\hat{S}_1(T,t) \to \hat{S}_1^{(0)}(T,t) = t^2\sqrt{AB + \frac{B^2}{12}T^2}$ when $R \to 0$.

Step 1: From (20), it suffices to prove that each element of $\boldsymbol{S}(T)$ is a monotonically increasing function of $R \in (0,\infty)$ for fixed $T \ge T_m$. If $R > 0$, then from the DARE in (17), it follows

$$\frac{S_1(T)R}{R-S_1(T)} = S_1(T) + 2TS_2(T) + T^2 S_3(T) + Q_1(T) \tag{33}$$

$$\frac{S_2(T)R}{R-S_1(T)} = S_2(T) + TS_3(T) + Q_2(T) \tag{34}$$

$$\frac{S_2^2(T)}{R-S_1(T)} = Q_3(T). \tag{35}$$

We then prove the monotonicity of $S_1(T)$, $S_2(T)$ and $S_3(T)$ with respect to R over $(0,\infty)$ one by one using contradictions. We first assume that $S_1(T)$ will decrease when R increases for some $R > 0$. From (35), we know that $S_2(T)$ will increase. From (33), it follows

$$S_3(T) = \frac{1}{T^2}\left(\frac{S_1^2(T)}{R-S_1(T)} - 2TS_2(T) - Q_1(T)\right). \tag{36}$$

Hence, $S_3(T)$ will decrease. From (33) and (34), we can obtain

$$S_3(T) = \frac{2TS_2^2(T) + S_2(T)Q_1(T) - S_1(T)Q_2(T)}{T(S_1(T) - TS_2(T))}. \tag{37}$$

It is noticed that the right-hand side (RHS) of (37) will increase, which implies that $S_3(T)$ will increase. This gives us a contradiction. Hence, we know $S_1(T)$ is a monotonically increasing function of $R > 0$. Next, we assume that $S_2(T)$ will decrease at some point $R > 0$. From (35), we know that $R - S_1(T)$ will decrease. Then, from (36), it follows that $S_3(T)$ will increase. However, the RHS of (37) will decrease, which is a contradiction. Hence, $S_2(T)$ is a monotonically increasing function of $R > 0$. Finally, we assume $S_3(T)$ will decrease at some point $R > 0$. From (34) and (35), we have $\frac{S_1(T)}{S_2(T)} = \frac{TS_3(T)+Q_2(T)}{Q_3(T)}$ which implies that $\frac{S_1(T)}{S_2(T)}$ will decrease. From (33) and (34), we have $\frac{S_1(T)}{S_2(T)} = \frac{2TS_2(T)}{TS_3(T)+Q_2(T)} + \frac{Q_1(T)-Q_2(T)T}{TS_3(T)+Q_2(T)} + T$. Note that both

the first term and the second term will increase and thus $\frac{S_1(T)}{S_2(T)}$ will increase, which is a contradiction, thus, $S_3(T)$ is a monotonically increasing function of R.

Step 2: From the DARE in (17), we can obtain a polynomial of $P_1(T)$ for fixed T as

$$\begin{aligned} &P_1^4(T) - (2U(T) + V(T))P_1^3(T) \\ &+ (U^2(T) - 2RU(T) - 5RV(T))P_1^2(T) \\ &+ (2RU^2(T) - 8R^2V(T))P_1(T) \\ &+ (R^2U^2(T) - 4R^3V(T)) = 0 \end{aligned} \tag{38}$$

where $U(T) = Q_1(T) - TQ_2(T)$ and $V(T) = T^2Q_3(T)$. Note that (38) is quartic in $P_1(T)$ for fixed T, it has four explicit solutions [50]. The *largest real* one is the (1,1) element of $\boldsymbol{P}(T)$, which is the unique solution of the DARE (17). To see this, we first use $P_1(T)$ to represent $P_2(T)$ and $P_3(T)$ as

$$P_2(T) = \sqrt{(P_1(T) + R)Q_3(T)} \tag{39}$$

$$P_3(T) = \frac{1}{T}\left(\frac{\sqrt{Q_3(T)}P_1(T)}{\sqrt{P_1(T) + R}} - Q_2(T)\right) + Q_3(T). \tag{40}$$

Hence, the determinant of $\boldsymbol{P}(T)$ is

$$|\boldsymbol{P}(T)| = \frac{P_1(T)}{T}\left(\frac{\sqrt{Q_3(T)}P_1(T)}{\sqrt{P_1(T)+R}} - Q_2(T)\right) - RQ_3(T).$$

It is noticed that $|\boldsymbol{P}(T)|$ is a monotonically increasing function of $P_1(T)$. Evidently, $P_1(T)$ should be real. If $P_1(T)$ is not the largest one among all the real solutions of (38) for fixed $T \geq T_m$, we then know that $\boldsymbol{P}(T)$ with $P_1(T)$ to be the largest real solution and $P_2(T)$ and $P_3(T)$ calculated by using (39) and (40), respectively, is also a positive definite solution of the DARE (17), which is a contradiction of the uniqueness of the solution. If $R = 0$, then from the DARE in (17), we can obtain a quadratic equation of $P_1(T)$. To distinguish the solution from that of $R > 0$, we use $P_1^{(0)}(T)$ to represent it. Among the two solutions of the quadratic equation, we choose $P_1^{(0)}(T) = \frac{(2U(T)+V(T))+\sqrt{4U(T)V(T)+V^2(T)}}{2}$ and discard the other one since we need $S_1^{(0)}(T) = P_1^{(0)}(T) - Q_1(T) > 0$. Recall that $P_1(T)$ is the largest real one of the four solutions of the quartic equation (38) for fixed $T \geq T_m$. If we allow R goes to zero in (38), then $P_1(T) \to P_1^{(0)}(T)$. From (19), (39) and (40), it follows $S_1(T) \to 0$, $S_2(T) \to 0$ and $S_3(T) \to \sqrt{AB + \frac{B^2}{12}T^2}$ when $R \to 0$. Therefore, $\hat{S}_1(T,t) \to \hat{S}_1^{(0)}(T,t) = t^2\sqrt{AB + \frac{B^2}{12}T^2}$ according to (20).

Combining **step 1** and **step 2**, it follows $\hat{S}_1(T,t) \geq \hat{S}_1^{(0)}(T,t)$ for any fixed $T \geq T_m$ and $t > 0$. This completes the proof of Lemma 2.

C. Proof of Proposition 1

If we define $\beta = \sqrt{\int_{t=0}^{\infty} e^{-2Q_1(t)}\,dt}$ and from (31), it follows $\int_{T_m}^{T} e^{-\sigma_\phi^2(T,t)}\,dt \leq \beta\sqrt{\int_0^{\infty} e^{-2\hat{S}_1^{(0)}(T,t)}\,dt}$ for all $T \in [T_m, \infty)$, where we use $\hat{S}_1(T,t) \geq \hat{S}_1^{(0)}(T,t)$ for any fixed $T \geq T_m$ and $t > 0$ from Lemma 2. We then substitute the expression of $\hat{S}_1^{(0)}(T,t)$ given in (25) into this inequality, it follows

$$\int_{T_m}^{T} e^{-\sigma_\phi^2(T,t)}\,dt \leq \frac{\beta}{\left(\frac{8}{\pi}\hat{S}_1^{(0)}(T,1)\right)^{\frac{1}{4}}} = \Lambda(T). \tag{41}$$

After plugging (41) into (7), we can obtain the expression of $\Phi(T_f)$ in (27). This completes the proof of Proposition 1.

D. Proof of Proposition 2

From (7), it suffices to show $\sigma_\phi^2(\mu_j T_f, t)$ is a continuous function of $T_f \in [T_m/\mu_{\min}, \infty)$ for any j and $t > 0$. In fact, we can show $\sigma_\phi^2(T,t)$ is a continuous function of $T > 0$ for any $t > 0$. From (20) and (21), it suffices to show each element of $\boldsymbol{S}(T)$ is a continuous function of $T > 0$. It then suffices to show that each element of $\boldsymbol{P}(T)$ is a continuous function of $T > 0$ according to (19) since each element of $\boldsymbol{S}(T)$ is a composition of continuous functions with respect to the elements of $\boldsymbol{P}(T)$. We give T a perturbation ΔT such that $T + \Delta T \in [T_m, \infty)$ and denote $\tilde{\boldsymbol{P}}(T)$ to be a symmetric solution of the following perturbed DARE:

$$\begin{aligned} \tilde{\boldsymbol{P}}(T) = \boldsymbol{F}(T+\Delta T)\left[\tilde{\boldsymbol{P}}(T) - \frac{\tilde{\boldsymbol{P}}(T)\boldsymbol{h}^{\mathrm{T}}\boldsymbol{h}\tilde{\boldsymbol{P}}(T)}{\boldsymbol{h}\tilde{\boldsymbol{P}}(T)\boldsymbol{h}^{\mathrm{T}} + R}\right]\boldsymbol{F}(T+\Delta T)^{\mathrm{T}} \\ + \boldsymbol{Q}(T+\Delta T). \end{aligned}$$

From Theorem 3.1 in [51], we have $||\tilde{\boldsymbol{P}}(T) - \boldsymbol{P}(T)||_F = O(\delta_{\boldsymbol{F},\boldsymbol{Q}})$ for $\delta_{\boldsymbol{F},\boldsymbol{Q}} \to 0$, where $\delta_{\boldsymbol{F},\boldsymbol{Q}} = (\|\Delta\boldsymbol{F}\|_F^2 + \|\Delta\boldsymbol{Q}\|_F^2)^{1/2}$ with $\Delta\boldsymbol{F} = \boldsymbol{F}(T + \Delta T) - \boldsymbol{F}(T)$ and $\Delta\boldsymbol{Q} = \boldsymbol{Q}(T + \Delta T) - \boldsymbol{Q}(T)$. When $\Delta T \to 0$, it follows $\delta_{\boldsymbol{F},\boldsymbol{Q}} \to 0$ since each element of either $\boldsymbol{F}(T)$ or $\boldsymbol{Q}(T)$ is a continuous function with respect to $T > 0$. Therefore, $\lim_{\Delta T \to 0} ||\tilde{\boldsymbol{P}}(T) - \boldsymbol{P}(T)||_F = 0$, which implies that each element of $\boldsymbol{P}(T)$ is a continuous function with respect to $T > 0$. This completes the proof of Proposition 2.

REFERENCES

[1] N. Tesla, "Apparatus for transmitting electrical energy," US Patent 1119732., Dec. 1914

[2] W. C. Brown, "The history of power transmission by radio waves," *IEEE Trans. Microw. Theory Tech.*, vol. 32, no. 9, pp. 1230–1242, Sept. 1984.

[3] Z. Ding et al., "Application of smart antenna technologies in simultaneous wireless information and power transfer," *IEEE Commun. Mag.*, vol. 53, no. 4, pp. 86–93, Apr. 2015.

[4] A. Sample and J. Smith, "Experimental results with two wireless power transfer systems," in *Proc. IEEE RWS*, Jan. 2009, pp. 16–18.

[5] A. Parks, A. Sample, Y. Zhao, and J. Smith, "A wireless sensing platform utilizing ambient RF energy," in *Proc. IEEE RWS*, Jan. 2013, pp. 331–333.

[6] V. Talla, B. Kellogg, B. Ransford, S. Naderiparizi, S. Gollakota, and J. R. Smith, "Powering the next billion devices with Wi-Fi," in *Proc. CoNEXT*, Dec. 2015, pp. 4:1–4:13.

[7] X. Wei and E. Li, "Simulation and experimental comparison of different coupling mechanisms for the wireless electricity transfer," *J. Electromagn. Waves Appl.*, vol. 23, no. 7, pp. 925–934, April 2009.

[8] E. Sazonov and M. R. Neuman, *Wearable Sensors: Fundamentals, Implementation and Applications.* Oxford: Academic Press, 2014.

[9] C.-G. Kim, D.-H. Seo, J.-S. You, J.-H. Park, and B.-H. Cho, "Design of a contactless battery charger for cellular phone," *IEEE Trans. Ind. Electron.*, vol. 48, no. 6, pp. 1238–1247, Dec. 2001.

[10] A. Tomar and S. Gupta, "Wireless power transmission: Applications and components," *Int. J. Eng. Research & Technology*, vol. 1, no. 5, July 2012.

[11] B. Lenaerts and R. Puers, *Omnidirectional Inductive Powering for Biomedical Implants.* Springer Publishing Company, Incorporated, 2008.

[12] T. Sun, X. Xie, and Z. Wang, *Wireless Power Transfer for Medical Microsystems.* Springer Publishing Company, Incorporated, 2013.
[13] André Kurs, Aristeidis Karalis, Robert Moffatt, J. D. Joannopoulos, Peter Fisher, Marin Soljačić, "Wireless power transfer via strongly coupled magnetic resonances," *Science*, vol. 317, no. 5834, pp. 83–86, 2007.
[14] S. Y. R. Hui, W. Zhong, and C. K. Lee, "A critical review of recent progress in mid-range wireless power transfer," *IEEE Trans. Power Electron.*, vol. 29, no. 9, pp. 4500–4511, Sept. 2014.
[15] J. Jadidian and D. Katabi, "Magnetic MIMO: How to charge your phone in your pocket," in *Proc. MobiCom*, 2014, pp. 495–506.
[16] M. R. V. Moghadam and R. Zhang, "Multiuser wireless power transfer via magnetic resonant coupling: Performance analysis, charging control, and power region characterization," *IEEE Trans. Signal Inf. Process. Over Netw.*, vol. 2, no. 1, pp. 72–83, March. 2016.
[17] G. Yang, M. R. V. Moghadam, and R. Zhang, "Magnetic beamforming for wireless power transfer," in *Proc. ICASSP*, Mar. 2016, pp. 3936–3940.
[18] J. O. Mur-Miranda, G. Fanti, Y. Feng, K. Omanakuttan, R. Ongie, A. Setjoadi, and N. Sharpe, "Wireless power transfer using weakly coupled magnetostatic resonators," in *Proc. IEEE ECCE*, Sept. 2010, pp. 4179–4186.
[19] "Tutorial overview of inductively coupled RFID systems," 2003. [Online]. Available: http://cdn.mobiusconsulting.com/papers/rfidsystems.pdf
[20] J. Murakami, F. Sato, T. Watanabe, H. Matsuki, S. Kikuchi, K. Harakawa, and T. Satoh, "Consideration on cordless power stationcontactless power transmission system," *IEEE Trans. Magnetics*, vol. 32, no. 5, pp. 5037–5039, Sept. 1996.
[21] R. Zhang and C. K. Ho, "MIMO broadcasting for simultaneous wireless information and power transfer," *IEEE Trans. Wireless Commun.*, vol. 12, no. 5, pp. 1989–2001, May 2013.
[22] X. Lu, P. Wang, D. Niyato, D. I. Kim, and Z. Han, "Wireless networks with RF energy harvesting: A contemporary survey," *IEEE Commun. Surveys Tuts.*, vol. 17, no. 2, pp. 757–789, 2015.
[23] L. Mohjazi, M. Dianati, G. Karagiannidis, S. Muhaidat, and M. Al-Qutayri, "RF-powered cognitive radio networks: Technical challenges and limitations," *IEEE Commun. Mag.*, vol. 53, no. 4, pp. 94–100, Apr. 2015.
[24] J. Xu, L. Liu, and R. Zhang, "Multiuser MISO beamforming for simultaneous wireless information and power transfer," *IEEE Trans. Signal Process.*, vol. 62, no. 18, pp. 4798–4810, Sept. 2014.
[25] J. Xu and R. Zhang, "Energy beamforming with one-bit feedback," *IEEE Trans. Signal Process.*, vol. 62, no. 20, pp. 5370–5381, Oct. 2014.
[26] R. Mudumbai, D. Brown, U. Madhow, and H. Poor, "Distributed transmit beamforming: Challenges and recent progress," *IEEE Commun. Mag.*, vol. 47, no. 2, pp. 102–110, Feb. 2009.
[27] R. Mudumbai, B. Wild, U. Madhow, and K. Ramch, "Distributed beamforming using 1 bit feedback: From concept to realization," in *Proc. Allerton Conference on Communication, Control, and Computing*, 2006.
[28] J. Hou, G. Yan, Z. Lin, and W. Xu, "Distributed transmit beamforming via feedback-based inter-cluster synchronization," in *Proc. IEEE CDC*, Dec. 2012, pp. 1392–1397.
[29] C. Lin, V. Veeravalli, and S. Meyn, "A random search framework for convergence analysis of distributed beamforming with feedback," *IEEE Trans. Inf. Theory*, vol. 56, no. 12, pp. 6133–6141, Dec. 2010.
[30] D.R. Brown III, P. Bidigare, and U. Madhow, "Receiver-coordinated distributed transmit beamforming with kinematic tracking," in *Proc. ICASSP*, Mar. 2012, pp. 5209–5212.
[31] D. Scherber et al., "Coherent distributed techniques for tactical radio networks: Enabling long range communications with reduced size, weight, power and cost," in *Proc.IEEE MILCOM*, Nov. 2013.
[32] R. Wang and D.R. Brown III, "Feedback rate optimization in receivercoordinated distributed transmit beamforming for wireless power transfer," in *Proc. CISS*, March 2015.
[33] R. Preuss and D.R. Brown III, "Retrodirective distributed transmit beamforming with two-way source synchronization," in *Proc. CISS*, March 2010, pp. 1–6.
[34] R. Mudumbai, S. Dasgupta, A. Kumar, B. Peiffer, U. Madhow, and D.R. Brown III, "Wideband retrodirective distributed transmit beamforming with endogenous relative calibration," in *Proc. ACSSC*, Nov. 2015.
[35] P. Bidigare, M. Oyarzun, D. Raeman, D. Cousins, D. Chang, R. ODonnell, and D.R. Brown III, "Implementation and demonstration of receivercoordinated distributed transmit beamforming across an adhoc radio network," in *Proc. ACSSC*, Nov. 2012, pp. 222–226.
[36] D. W. K. Ng and R. Schober, "Secure and green SWIPT in distributed antenna networks with limited backhaul capacity," *IEEE Trans. Wireless Commun.*, vol. 14, no. 9, pp. 5082–5097, Sept. 2015.
[37] Z. Fang, X. Yuan, and X. Wang, "Distributed energy beamforming for simultaneous wireless information and power transfer in the two-way relay channel," *IEEE Signal Process Lett.*, vol. 22, no. 6, pp. 656–660, June 2015.
[38] D. R. Jones, C. D. Perttunen, and B. E. Stuckman, "Lipschitzian optimization without the lipschitz constant," *J. Optim. Theory Appl.*, vol. 79, no. 1, pp. 157–181, Oct. 1993.
[39] G. Giorgi and C. Narduzzi, "Performance analysis of kalman-filterbased clock synchronization in ieee 1588 networks," *IEEE Trans. Instrum. Meas.*, vol. 60, no. 8, pp. 2902–2909, Aug. 2011.
[40] D.R. Brown III and R. David, "Receiver-coordinated distributed transmit nullforming with local and unified tracking," in *Proc. ICASSP*, May 2014, pp. 1160–1164.
[41] S. Stein and R. Filler, "Kalman filter analysis for real time applications of clocks and oscillators," in *Proc. of the 42nd Annual Frequency Control Symposium*, June 1988, pp. 447–452.
[42] Y. Shmaliy, "An unbiased fir filter for tie model of a local clock in applications to gps-based timekeeping," *IEEE Trans. Ultrason., Ferroelectr., Freq. Control*, vol. 53, no. 5, pp. 862–870, May 2006.
[43] Y. Bar-Shalom, X. Rong Li, and T. Kirubarajan, *Estimation with Applicatins to Tracking and Navigation.* John Wiley and Sons, 2001.
[44] R. Mehra, "On the identification of variances and adaptive kalman filtering," *IEEE Trans. Autom. Control*, vol. 15, no. 2, pp. 175–184, Apr 1970.
[45] "Rakon RFPO45 crystal oscillator datasheet," 2009. [Online]. Available: http://www.rakon.com/Products/Public/Documents/Specifications/RFPO45.pdf
[46] W. Klepczynski and P. Ward, "Frequency stability requirements for narrow band receivers," *32nd Annual Precise Time and Time Interval Meeting*, Nov. 2000.
[47] R. P. Brent, "An algorithm with guaranteed convergence for finding a zero of a function," *The Computer Journal*, vol. 14, no. 4, pp. 422–425, 1971.
[48] W. H. Press, S. A. Teukolsky, W. T. Vetterling, and B. P. Flannery, *Numerical Recipes 3rd Edition: The Art of Scientific Computing.* Cambridge University Press, 2007.
[49] S. Cui, A. Goldsmith, and A. Bahai, "Energy-constrained modulation optimization," *IEEE Trans. Wireless Commun.*, vol. 4, no. 5, pp. 2349–2360, Sept. 2005.
[50] M. Abramowitz, *Handbook of Mathematical Functions, With Formulas, Graphs, and Mathematical Tables.* Dover Publications, Incorporated, 1974.
[51] J. Sun, "Sensitivity analysis of the discrete-time algebraic riccati equation," *Linear Algebra and its Applications*, vol. 275–276, pp. 595–615, 1998.

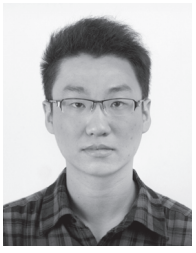

Rui Wang (S'15) received the B.S. degree in Electrical Engineering from Nanjing University of Aeronautics and Astronautics (NUAA), China, in 2011. He received the M.S. degree in Electrical and Computer Engineering from Worcester Polytechnic Institute in 2013. He is currently a Ph.D. candidate at Worcester Polytechnic Institute. His research interests are currently in coordinated wireless transmission and reception, synchronization, and wireless power transfer.

D. Richard Brown III (S'97-M'00-SM'09) received the B.S. and M.S. degrees from the University of Connecticut in 1992 and 1996, respectively, and the Ph.D. degree from Cornell University in 2000, all in electrical engineering. From 1992 to 1997, he was with General Electric Electrical Distribution and Control. He joined as a Faculty Member at the Worcester Polytechnic Institute, Worcester, MA, USA, in 2000. He was a Visiting Associate Professor with Princeton University from 2007 to 2008. Since 2016, He has been with the National Science Foundation as a Program Director in the Computing and Communication Foundations Division.